

Haverford College

Haverford Scholarship

Faculty Publications

Astronomy

2002

The Large-scale Structure of the X-ray Background and Its Cosmological Implications

Stephen P. Boughn

Haverford College, sboughn@haverford.edu

R. G. Crittenden

Greg Koehrsen '00

Class of 2000, Haverford College

Follow this and additional works at: https://scholarship.haverford.edu/astronomy_facpubs

Repository Citation

"The Large-scale Structure of the X-ray Background and Its Cosmological Implications" (with R. Crittenden and G. Koehrsen), *Ap. J.*, 580, 672 (2002).

This Journal Article is brought to you for free and open access by the Astronomy at Haverford Scholarship. It has been accepted for inclusion in Faculty Publications by an authorized administrator of Haverford Scholarship. For more information, please contact nmedeiro@haverford.edu.

THE LARGE-SCALE STRUCTURE OF THE X-RAY BACKGROUND AND ITS COSMOLOGICAL IMPLICATIONS

S. P. BOUGHN

Department of Astronomy, Haverford College, Haverford, PA 19041; sboughn@haverford.edu

R. G. CRITTENDEN

Department of Applied Mathematics and Theoretical Physics, University of Cambridge, Cambridge CB3 9EW, UK;
r.g.crittenden@damtp.cam.ac.uk

AND

G. P. KOEHRSEN

Department of Astronomy, Haverford College, Haverford, PA 19041; gregory.koehrsen@westtown.edu

Received 2002 July 9; accepted 2002 August 1

ABSTRACT

A careful analysis of the *HEAO 1 A-2* 2–10 keV full-sky map of the X-ray background (XRB) reveals clustering on the scale of several degrees. After removal of the contribution due to beam smearing, the intrinsic clustering of the background is found to be consistent with an autocorrelation function of the form $(3.6 \pm 0.9) \times 10^{-4} \theta^{-1}$, where θ is measured in degrees. If current active galactic nucleus models of the hard XRB are reasonable and the cosmological constant–cold dark matter (Λ CDM) cosmology is correct, this clustering implies an X-ray bias factor of $b_X \sim 2$. Combined with the absence of a correlation between the XRB and the cosmic microwave background (CMB), this clustering can be used to limit the presence of an integrated Sachs-Wolfe (ISW) effect and thereby to constrain the value of the cosmological constant, $\Omega_\Lambda \leq 0.60$ (95% CL). This constraint is inconsistent with much of the Ω_Λ parameter space currently favored by other observations. Finally, we marginally detect the dipole moment of the diffuse XRB and find it to be consistent with the dipole due to our motion with respect to the mean rest frame of the XRB. The limit on the amplitude of any intrinsic dipole is $\delta I/I \leq 5 \times 10^{-3}$ at the 95% CL. When compared to the local bulk velocity, this limit implies a constraint on the matter density of the universe of $\Omega_m^{0.6}/b_X(0) \gtrsim 0.24$.

Subject headings: large-scale structure of universe — X-rays: diffuse background — X-rays: galaxies — X-rays: general

On-line material: color figures

1. INTRODUCTION

The X-ray background (XRB) was discovered before the cosmic microwave background (CMB), but only now is its origin being fully understood. The hard (2–10 keV) XRB has been nearly completely resolved into individual sources; most of these are active galactic nuclei (AGNs), but there is a minor contribution from the hot, intergalactic medium in rich clusters of galaxies (Rosati et al. 2002; Cowie et al. 2002; Mushotzky et al. 2000). In addition, the spectra of these faint X-ray sources are consistent with that of the “diffuse” XRB. If current models of the luminosity functions and evolution of these sources are reasonably correct, then the XRB arises from sources in the redshift range $0 < z < 4$, making them an important probe of density fluctuations intermediate between relatively nearby galaxy surveys ($z \lesssim 0.5$) and the CMB ($z \sim 1000$).

While there have been several attempts to measure large-scale, correlated fluctuations in the hard XRB, these have yielded only upper limits or, at best, marginal detections (e.g., Barcons et al. 2001; Treyer et al. 1998 and references therein). On small scales, a recent correlation analysis of 159 sources in the *Chandra* Deep Field South survey detected significant correlations for separations out to 100'' (Giacconi et al. 2001). (At the survey flux level, these sources comprise roughly two-thirds of the hard XRB.) On much larger scales, a recent analysis by Scharf et al. (2000) claims

a significant detection of large-scale harmonic structure in the XRB with spherical harmonic order $1 \leq \ell \leq 10$ corresponding to structures on angular scales of $\theta \gtrsim 10^\circ$. The autocorrelation results we describe here complement this analysis, indicating clustering on angular scales of 3° – 10° , corresponding to harmonic order of $\ell \lesssim 30$. However, all three detections have relatively low signal-to-noise ratio and require independent confirmation.

The dipole moment of the XRB has received particular attention, primarily because of its relation to the dipole in the CMB, which is likely due to the Earth’s motion with respect to the rest frame of the CMB. If this is the case, one expects a similar dipole in the XRB with an amplitude that is 3.4 times larger because of the difference in spectral indices of the two backgrounds (Boldt 1987). In the X-ray literature, this dipole is widely known as the Compton-Getting effect (Compton & Getting 1935). In addition, it is quite likely that the XRB has an intrinsic dipole due to the asymmetric distribution in the local matter density that is responsible for the Earth’s peculiar motion in the first place. Searches for both these dipoles have concentrated on the hard XRB, since at lower energies the X-ray sky is dominated by Galactic structure. There have been several tentative detections of the X-ray dipole (e.g., Scharf et al. 2000), but these have large uncertainties. A firm detection of an intrinsic dipole or even an upper limit on its presence would provide an important constraint on the inhomogeneity of

the local distribution of matter via a less often used tracer of mass and a concomitant constraint on cosmological models (e.g., Lahav, Piran, & Treyer 1997).

This paper is organized as follows. In § 2 we describe the hard X-ray map used in the analysis, the determination of its effective beam size, and cuts made to remove the foreground contaminants. In § 3, we describe the remaining large-scale structures in the map and the determination of their amplitudes. The dipole is of particular interest and is the topic of § 4. The correlation function of the residual map and its implications for intrinsic correlations are discussed in § 5. In § 6, we compare our results to previous observations and discuss the cosmological implications of these results in § 7.

2. *HEAO 1* A-2 2–10 keV X-RAY MAP

There has been much recent progress in understanding the XRB through instruments such as *ROSAT*, *Chandra*, and *XMM*. However, these either have too low an energy threshold or have too small a field of view to study the large-scale structure of the hard X-rays. The best observations relevant to large-scale structure are still those from the *HEAO 1* A-2 experiment that measured the surface brightness of the XRB in the 0.1–60 keV band (Boldt 1987).

The *HEAO 1* data set we consider was constructed from the output of two medium-energy detectors (MED) with different fields of view ($3^\circ \times 3^\circ$ and $3^\circ \times 1.5^\circ$) and two high-energy detectors (HED3) with these same fields of view. These data were collected during the 6 month period beginning on day 322 of 1977. Counts from the four detectors were combined and binned in 24,576 1.3×1.3 pixels. The pixelization we use is an equatorial quadrilateralized spherical cube projection on the sky, the same as used for the

COBE satellite CMB maps (White & Stemwedel 1992). The combined map has a spectral bandpass (quantum efficiency $\gtrsim 50\%$) of approximately 3–17 keV (Jahoda & Mushotzky 1989) and is shown in Galactic coordinates in Figure 1. For consistency with other work, all signals are converted to equivalent flux in the 2–10 keV band.

Because of the ecliptic longitude scan pattern of the *HEAO* satellite, sky coverage and therefore photon shot noise are not uniform. However, the variance of the cleaned, corrected map, 2.1×10^{-2} (TOT counts s^{-1})², is much larger than the variance of photon shot noise, 0.8×10^{-2} (TOT counts s^{-1})², where 1 TOT counts $s^{-1} \approx 2.1 \times 10^{-11}$ ergs $s^{-1} \text{ cm}^{-2}$ (Allen, Jahoda, & Whitlock 1994). This implies that most of the variance in the X-ray map is due to “real” structure. For this reason and to reduce contamination from any systematics that might be correlated with the scan pattern, we chose to weight the pixels equally in this analysis.

2.1. The Point-Spread Function

To determine the level of intrinsic correlations, we must account for the effects of beam smearing, so it is essential to characterize the point-spread function (PSF) of the above map. The PSF varies somewhat with position on the sky because of the pixelization and the asymmetric beam combined with the *HEAO 1* scan pattern. We obtained a mean PSF by averaging the individual PSFs of 60 strong *HEAO 1* point sources (Piccinotti et al. 1982) that were located more than 20° from the Galactic plane. The latter condition was imposed to avoid crowding and to approximate the windowing of the subsequent analysis (see § 2.2). The composite PSF, shown in Figure 2, is well fitted by a Gaussian with an FWHM of $3''.04$.

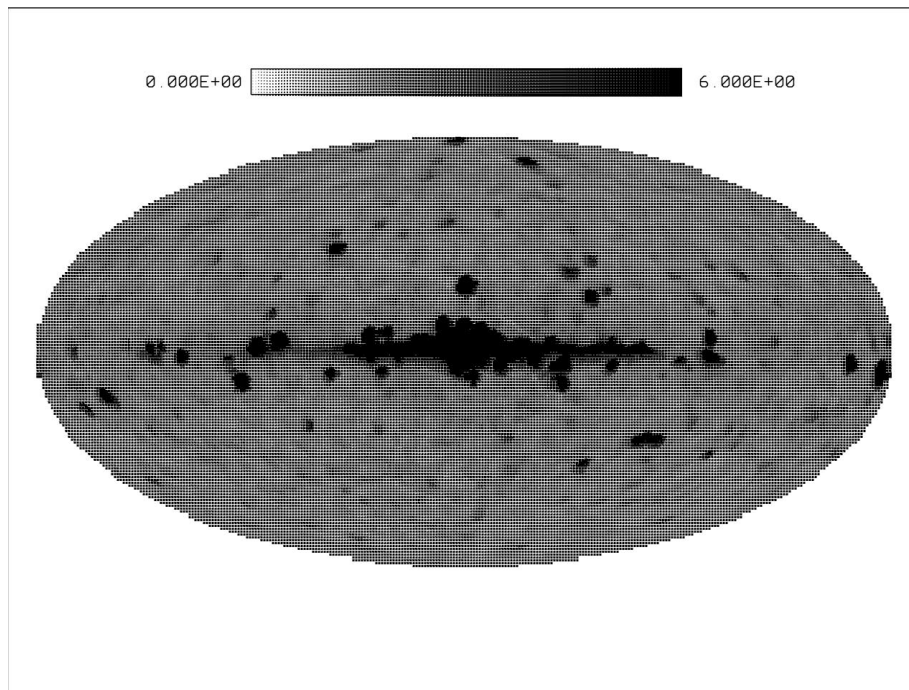


FIG. 1.—Combined map from the *HEAO 1* A-2 medium- and high-energy detectors, pixelized using the standard *COBE* quad cubed format (1.3×1.3 pixels.) The effective beam size is approximately 3° . The most visible features, the Galactic plane and the nearby bright sources, are removed from the maps we analyze. The units are TOT counts s^{-1} (4.5 deg^2)⁻¹.

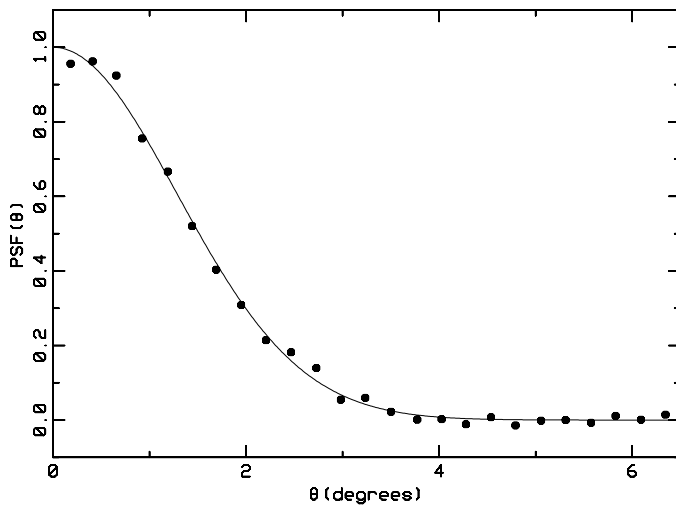


FIG. 2.—Mean PSF for the combined map found by averaging the individual PSFs of 60 strong *HEAO 1* point sources. The data are well fitted by a Gaussian with FWHM of $3^{\circ}04$.

As a check of this PSF, we generated Monte Carlo maps of sources observed with $3^{\circ} \times 3^{\circ}$ and $3^{\circ} \times 1^{\circ}5$ (FWHM) triangular beams appropriate for the A-2 detectors (Shafer 1983) and then combined the maps with quad cubed pixelization as above. The resulting average PSF from these trials is also well fitted by a Gaussian with an FWHM of $2^{\circ}91$, i.e., about 4.5% less than that in Figure 2. Considering that the widths of the triangular beams given above are nominal, that the triangular beam pattern is only approximate (especially at higher energies), and that we did not take into account the slight smearing in the satellite scan direction (Shafer 1983), the agreement is remarkably good. In the following analysis, we use the $3^{\circ}04$ fit derived from the observed map; however, changing the PSF FWHM by a few percent does not significantly affect the results of this paper.

2.2. Cleaning the Map

To remove the effects of the Galaxy and strong extragalactic point sources, some regions of the map were excluded from the analysis. The dominant feature in the *HEAO* map is the Galaxy (see Fig. 1), so all data within 20° of the Galactic plane or within 30° of the Galactic center were cut from the map. In addition, large regions ($6^{\circ}5 \times 6^{\circ}5$) centered on 92 discrete X-ray sources with 2–10 keV fluxes larger than 3×10^{-11} ergs s^{-1} cm^{-2} (Piccinotti et al. 1982) were removed from the maps. Around the 16 brightest of these sources (with fluxes larger than 1×10^{-10} ergs s^{-1} cm^{-2}) the cut regions were enlarged to $9^{\circ} \times 9^{\circ}$. Further enlarging the area of the excised regions had a negligible effect on the following analysis, so we conclude that the sources have been effectively removed. The resulting “cleaned” map (designated map A) has a sky coverage of 55.5% and is our baseline map for further cuts.

To test the possibility of further point-source contamination, we also used the *ROSAT* All-Sky Survey (RASS) Bright Source Catalog (Voges et al. 1996) to identify relatively bright sources. While the RASS survey has somewhat less than full sky coverage (92%), it has a relatively low flux limit that corresponds to a 2–10 keV flux of $\sim 2 \times 10^{-13}$ ergs s^{-1} cm^{-2} for a photon spectral index of $\alpha = -2$. Every source in the RASS catalog was assigned a

2–10 keV flux from its B-band flux by assuming a spectral index of $-3 < \alpha < -1$ as deduced from its HR2 hardness ratio. For fainter sources, the computed value of α is quite uncertain; if it fell outside the typical range of most X-ray sources, $-3 < \alpha < -1$, then α was simply forced to be -1 or -3 . It is clear that extrapolating RASS flux to the 2–10 keV band is not accurate, so one must consider the level to which sources are masked with due caution. However, we are using these fluxes only to mask bright sources, so this procedure is unlikely to bias the results.

We considered maps where the *ROSAT* sources were removed at three different inferred 2–10 keV flux thresholds. First, we identified sources with fluxes exceeding the Piccinotti level, 3×10^{-11} ergs s^{-1} cm^{-2} . Thirty-four additional, high Galactic latitude RASS sources were removed, resulting in a map with sky coverage of 52% (designated map B). In order to compare more directly with the results of Scharf et al. (2000) (see § 6) we removed sources at their flux level, 2×10^{-11} ergs s^{-1} cm^{-2} . The map masked in this way has 47% sky coverage (compared to the 48% coverage of the Scharf et al. analysis) and is designated map C. Finally, to check how sensitive our dipole results are to the particular masking of the map, we lowered the flux cut level to 1×10^{-11} ergs s^{-1} cm^{-2} , which reduced the sky coverage to 34%. The map resulting from this cut is designated map D in Table 3.

As an alternative to using the RASS sources, the map itself was searched for “sources” that exceeded the nearby background by a specified amount. Since the quad cubed format lays out the pixels on an approximately square array, we averaged each pixel with its eight neighbors and then compared this value with the median value of the next nearest 16 pixels (ignoring pixels within the masked regions). If the average flux associated with a given pixel exceeded the median flux of the background by a prescribed threshold, then all 25 pixels ($6^{\circ}5 \times 6^{\circ}5$) were removed from further consideration. For a threshold corresponding to 2.2 times the mean shot noise in the map approximately 120 more “sources” were identified and masked, resulting in a sky coverage of 42%. This map is labeled map E in Table 3. Finally, we used an even more aggressive cut corresponding to 1.75 times the mean shot noise, which resulted in a masked map with 33% sky coverage. This map is labeled map F.

3. MODELING THE LOCAL LARGE-SCALE STRUCTURE

3.1. Sources of Large-Scale Structure

There are several local sources of large-scale structure in the *HEAO* map that cannot be eliminated by masking isolated regions. These include diffuse emission from the Galaxy, emission (diffuse and/or faint point sources) from the Local Supercluster, the Compton-Getting dipole, and a linear time drift in detector sensitivity. Since none of these are known a priori, we fit an eight-parameter model to the data. Of course, the Compton-Getting dipole is known in principle if one assumes the kinetic origin of the dipole in the CMB; however, there may also be an intrinsic X-ray dipole that is not accounted for. (See § 4 below.) Only one correction was made a priori to the map, and that was for the dipole due to the Earth’s motion around the Sun; however,

this correction has a negligible effect on the results. A more detailed account of the model is given in Boughn (1999).

The XRB has a diffuse (or unresolved) Galactic component that varies strongly with Galactic latitude (Iwan et al. 1982). This emission is still significant at high Galactic latitude ($b_{\text{II}} > 20^\circ$) and extrapolates to $\sim 1\%$ at the Galactic poles. We modeled this emission in two ways. The first model consisted of a linear combination of a secant law Galaxy with the Haslam 408 GHz full-sky map (Haslam et al. 1982). The latter was included to take into account X-rays generated by inverse Compton scattering of CMB photons from high-energy electrons in the Galactic halo, the source of much of the synchrotron emission in the Haslam map. As an alternative Galaxy model we also considered the two-disk, exponentially truncated model of Iwan et al. (1982). Our results are independent of which model is used.

In addition to the Galactic component, evidence has been found for faint X-ray emission from the plane of the Local Supercluster (Jahoda 1993; Boughn 1999). Because of its faintness, very detailed models of this emission are not particularly useful. The model we use here is a simple “pillbox,” i.e., uniform X-ray emissivity within a circular disk of thickness equal to $\frac{1}{4}$ the radius and with its center located $\frac{4}{5}$ of a radius from us in the direction of the Virgo Cluster (see Boughn 1999 for details). The amplitude of this emission, while significant, is largely independent of the details of the model and, in any case, has only a small effect on the results.

Time drifts in the detector sensitivity can also lead to apparent structure in the reconstructed X-ray map. At least one of the A-2 detectors changed sensitivity by $\sim 1\%$ in the 6 month interval of the current data set (Jahoda 1993). Because of the ecliptic scan pattern of the *HEAO* satellite, this results in a large-scale pattern in the sky that varies with ecliptic longitude with a period of 180° . If the drift is assumed to be linear, the form of the resulting large-scale structure in the map is completely determined. A linear drift of unknown amplitude is taken into account by constructing a sky map with the appropriate structure and then fitting for the amplitude simultaneously with the other parameters. We investigated the possibility of nonlinear drift by considering quadratic and cubic terms as well; however, this did not significantly reduce the χ^2 of the fit nor change the subsequent results.

3.2. Modeling the Maps

The eight parameters that characterize the amplitude of these structures are used to model the large-scale structure in the *HEAO* map. Let the X-ray intensity map be denoted by the vector \mathbf{I} , where the element I_i is the intensity in the i^{th} pixel. The observed intensity is modeled as the sum of eight templates with amplitudes described by the eight-dimensional vector \mathbf{a} ,

$$\mathbf{I} = \tilde{\mathbf{X}}\mathbf{a} + \mathbf{n}, \quad (1)$$

where $\tilde{\mathbf{X}}$ is an $8 \times n_{\text{pix}}$ matrix whose elements are the values of each template function at each pixel of the map. As discussed above, these template functions include a uniform map to represent the monopole of the XRB, the three components of a dipole (in equatorial coordinates), the large-scale pattern resulting from a linear instrumental gain drift, a Galactic secant law, the Haslam 408 GHz map, and the amplitude of the “pillbox” model of the Local Super-

cluster. The noise vector \mathbf{n} is assumed to be Gaussian distributed with correlations described by $\tilde{\mathbf{C}} \equiv \langle \mathbf{n}\mathbf{n}^T \rangle$.

As discussed above (§ 2), we chose to weight each pixel equally since the shot noise is considerably less than the “real” fluctuations in the sky. For the purposes of fitting the map to the above model, we consider both photon shot noise and fluctuations in the XRB (see Fig. 3) to be “noise.” This noise is correlated, and a minimum χ^2 fit must take such correlations into account. However, for simplicity, we ignore these correlations when finding the best-fit model amplitudes and perform a standard least-squares fit by minimizing $|\mathbf{I} - \tilde{\mathbf{X}}\mathbf{a}|^2$ on the cleaned *HEAO* map. From the standard equations of linear regression the values of the parameters that minimize this sum are

$$\mathbf{a} = \tilde{\mathbf{B}}^{-1} \tilde{\mathbf{X}}^T \mathbf{I}, \quad (2)$$

where $\tilde{\mathbf{B}} = \tilde{\mathbf{X}}^T \tilde{\mathbf{X}}$ is a symmetric eight by eight matrix. This would be the maximum likelihood estimator if the correlation matrix were uniform and diagonal. Although this fit ignores correlations in the errors, it is unbiased and is likely to be very close to the minimum χ^2 (maximum likelihood) fit, since the noise correlations are on a much smaller scale than the features we are attempting to fit.

The correlated nature of the noise cannot be ignored when the uncertainties in the fit are computed since there are far fewer noise-independent data points than there are pixels in the map. It is straightforward to show that errors in the estimated parameters $\delta\mathbf{a}$ are given by

$$\langle \delta\mathbf{a}\delta\mathbf{a}^T \rangle = \tilde{\mathbf{B}}^{-1} \tilde{\mathbf{X}}^T \tilde{\mathbf{C}} \tilde{\mathbf{X}} \tilde{\mathbf{B}}^{-1}. \quad (3)$$

This error is likely to be only slightly larger than would be the case for the maximum likelihood estimator. $\tilde{\mathbf{C}}$ is a combination of the uncorrelated shot noise and the correlated fluctuations indicated in Figure 3. We assume it to be homogeneous and isotropic, i.e., that \tilde{C}_{ij} depends only on the angular separation of the i and j pixels.

Table 1 lists the values and errors of the parameters fitted to map C (see § 2). Instrument time drift, the Galaxy, and

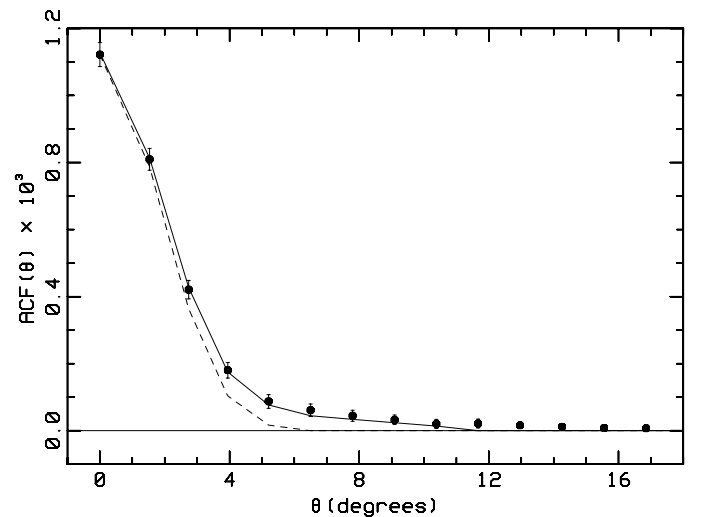


FIG. 3.—Autocorrelation function of the *HEAO 1* A-2 map with bright sources and the Galactic plane removed and corrected for large-scale, high Galactic latitude structure. The dashed curve is that expected from beam smearing due to the PSF of the map, while the solid curve includes a contribution due to clustering in the XRB (see § 5).

TABLE 1
EIGHT FIT PARAMETERS FOR MAP C

Component	Parameter	Uncorrected	Corrected for C-G
a_1	Background	328.6 ± 1.9	Same
a_2	\hat{x} dipole	-1.17 ± 0.62	-0.24 ± 0.62
a_3	\hat{y} dipole	-0.38 ± 0.98	-0.68 ± 0.98
a_4	\hat{z} dipole	-0.52 ± 0.69	-0.34 ± 0.69
a_5	Time drift	7.15 ± 1.23	Same
a_6	Secant law	3.28 ± 0.84	Same
a_7	Haslam map	0.03 ± 0.08	Same
a_8	Supercluster	4.11 ± 1.35	Same

NOTE.—Sources brighter than 2×10^{-11} ergs s^{-1} cm^{-2} have been removed. The units are 0.01 TOT counts $s^{-1}(4.5 \text{ deg}^2)^{-1} \simeq 1.54 \times 10^{-10}$ ergs s^{-1} cm^{-2} . Fits are shown both for the original map and for the map corrected for the Compton-Getting (C-G) dipole.

structure associated with the Local Supercluster all appear to be significant detections. The dipole is detected at about the 2σ level and is consistent with that expected for the Compton-Getting dipole (see Table 3). Table 2 lists the elements of the normalized correlation matrix of the fit parameters, and it is apparent that the parameters are largely uncorrelated. This was supported by fits that excluded some of the parameters (see § 4).

To compute the true $\chi^2 \equiv (\mathbf{I} - \tilde{\mathbf{X}}\mathbf{a})^T \tilde{\mathbf{C}}^{-1} (\mathbf{I} - \tilde{\mathbf{X}}\mathbf{a})$ of the fit requires inverting $\tilde{\mathbf{C}}$, which is an 11, 531 \times 11, 531 matrix. Instead we compute an effective reduced χ^2 using

$$\chi_{\text{eff}}^2 \equiv \frac{1}{N} (\mathbf{I} - \tilde{\mathbf{X}}\mathbf{a})^T \tilde{\mathbf{D}}^{-1} (\mathbf{I} - \tilde{\mathbf{X}}\mathbf{a}), \quad (4)$$

where $\tilde{\mathbf{D}}$ is the diagonal part of the correlation matrix, $\tilde{D}_{ii} = \sigma_{s,i}^2 + \sigma_b^2$, $\sigma_{s,i}$ is the shot noise in the i^{th} pixel, σ_b^2 is the variance of the fluctuations in the XRB, and N is the number of pixels minus 8, the number of degrees of freedom in the fit. The shot noise in a given pixel is inversely proportional to the number of photons received and we assume is inversely proportional to the coverage of that pixel. This is approximately true since all the nonflagged pixels are exposed to approximately the same flux. We find $\chi_{\text{eff}}^2 = 1.00$ for this fit, which we take as an indication that we have properly characterized the amplitude of the noise so that the errors quoted in the table have neither been underestimated nor overestimated. However, it should be emphasized that χ_{eff}^2 is not to be interpreted statistically as being derived from a χ^2 distribution.

The residual maps show very little evidence for structure on angular scales $\theta > 10^\circ$ above the level of the noise,

TABLE 2
NORMALIZED CORRELATION COEFFICIENTS FOR THE FIT
PARAMETERS IN TABLE 1

	a_1	a_2	a_3	a_4	a_5	a_6	a_7	a_8
a_1	1.0	0.0	-0.5	0.1	-0.4	-0.6	-0.1	-0.3
a_2	0.0	1.0	-0.1	0.2	0.3	-0.1	0.0	0.1
a_3	-0.5	-0.1	1.0	0.1	0.0	0.7	0.0	-0.3
a_4	0.1	0.2	0.1	1.0	-0.1	0.0	0.0	-0.1
a_5	-0.4	0.3	0.0	-0.1	1.0	0.0	0.0	0.2
a_6	-0.6	-0.1	0.7	0.0	0.0	1.0	0.0	-0.4
a_7	-0.1	0.0	0.0	0.0	0.0	0.0	1.0	-0.3
a_8	-0.3	0.1	-0.3	-0.1	0.2	-0.4	-0.3	1.0

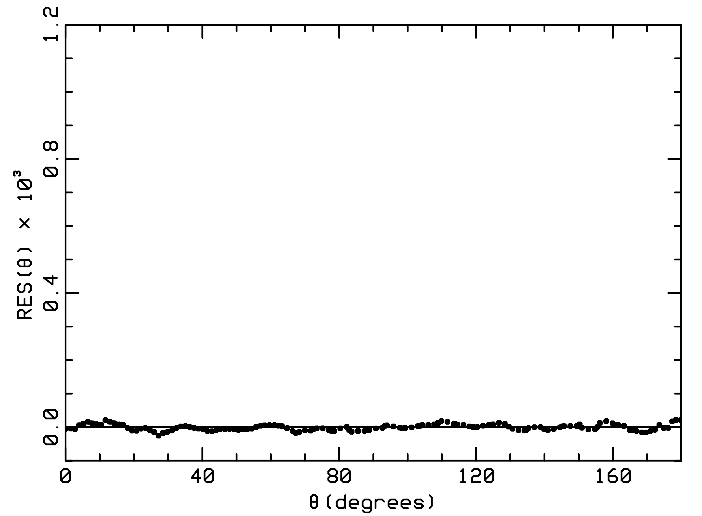


FIG. 4.—Residuals of the ACF fit from Fig. 3, after the shot noise, PSF, and a simple model of the intrinsic fluctuations have been removed.

$\langle \delta I^2 \rangle / \bar{I}^2 \sim 10^{-5}$, where δI are the residual fluctuations in X-ray intensity and \bar{I} is the mean intensity (see Fig. 4). Since all the components of the model have significant structure on large angular scales, it seems that these particular systematics have been effectively eliminated.

4. THE DIPOLE OF THE X-RAY BACKGROUND

The dipole fit to the map is consistent with the Compton-Getting dipole, and there is no evidence for any additional intrinsic dipole in the XRB. To make this more quantitative, we corrected the maps for the predicted Compton-Getting dipole and fitted the corrected map for any residual, intrinsic dipole. These dipole fit parameters are also included in Table 1.

Leaving out any individual model component, such as the time drift, the galaxy, Haslam or supercluster template, made little difference in the amplitude of the fit dipole. This is, perhaps, not too surprising since the Galaxy and time drift models are primarily quadrupolar in nature and the pancake model, while possessing a significant dipole moment, has a relatively small amplitude. All such fits were consistent with the Compton-Getting dipole alone. Even when all four of these parameters were excluded from the fit, the dipole amplitude increased by only 0.004 TOT counts s^{-1} with a direction that was 33° from that of the CMB dipole. The effective χ^2 for the four-parameter fit was, however, significantly worse, i.e., $\chi_{\text{eff}}^2 = 1.05$.

Table 3 lists the amplitude and direction of the dipole fit to map C along with the fits to maps D, E, and F. All these fits are consistent with amplitude and direction of the Compton-Getting dipole (as inferred from the CMB dipole), which is also indicated in the table. The effective χ^2 of these fits range from 0.99 to 1.01, again indicating that the amplitude of the noise is reasonably well characterized. No errors are given for these quantities for reasons that will be discussed below. In order to check for unknown systematics, we performed dipole fits to a variety of other masked maps with larger Galaxy cuts as well as cuts of the brighter galaxies in the Tully Nearby Bright Galaxy Atlas (Tully 1988). The details of these cuts are discussed in Boughn (1999); however, none had a significantly different dipole fit.

TABLE 3
DIPOLE AMPLITUDES OF VARIOUS MAPS

Map	Dipole	l_{II} (deg)	b_{II} (deg)	Constrained Dipole
Map C.....	0.0133	309	39	0.0117 ± 0.0064
Map D.....	0.0218	300	33	0.0184 ± 0.0062
Map E.....	0.0150	296	50	0.0148 ± 0.0059
Map F.....	0.0190	283	44	0.0184 ± 0.0064
C-G.....	0.0145	264	48	0.0145

NOTE.—The dipole amplitude and directions are from the eight-parameter fits in TOT units and Galactic coordinates. Map C is for the map of Table 1; Map D is masked at a source level of $\sim 1 \times 10^{-11}$ ergs s $^{-1}$ cm $^{-2}$; Map E is masked with internal source identification; and Map F is masked with a lower level of internal source identification (see § 2 for full details). Also listed are the amplitude and direction of the Compton-Getting dipole as inferred from the CMB dipole. The constrained amplitudes are for dipole models fixed to the direction of the CMB dipole.

Since all of these dipoles are consistent with the Compton-Getting dipole, we also fitted these maps with a six-parameter model in which the dipole direction was constrained to be the direction of the CMB dipole. The dipole amplitude of these fits and errors computed according to equation (3) are also given in Table 3.

Even though we find no evidence for an intrinsic dipole in the XRB, it would be useful to place an upper limit on its amplitude. We define the dimensionless dipole by writing the first two moments of the X-ray intensity as

$$I(\hat{n}) = \bar{I}(1 + \Delta \cdot \hat{n}), \quad (5)$$

where Δ is a vector in the direction of the dipole. There are various approaches one could take to find an upper limit, and the problem is complicated somewhat because the error bars are anisotropic (see Table 1). The dipole in the \hat{y} direction is less constrained than in the other directions because of the anisotropic masking of the map. Here we take the limits on the individual components of the intrinsic dipole and marginalize over the dipole direction to obtain a distribution for its amplitude. For this, we use a Bayesian formalism and assume a uniform prior on the amplitude, $|\Delta|$. We find $\Delta < 0.0052$ at the 95% CL. If the direction of the dipole is fixed to be that of the CMB dipole, then the 95% CL upper limits on the dipole amplitudes fall in the range 0.0030–0.0043 for the fits listed in Table 3.

The same sort of problem arises when one tries to attach an error bar to the amplitude of the dipole fits to the maps that include the Compton-Getting dipole. It seems clear from Table 1 that we find evidence for a dipole at the 2σ level. This is supported by the six-parameter fits of Table 3, where the various maps indicate positive detections at a 2–3 σ level. However, in the eight-parameter fits, the dipole amplitude is a nonlinear combination of the fit components. There are two approaches we can take in converting the three-dimensional limits to a limit on the dipole amplitude. We can either fix the direction in the direction of the CMB dipole, which results in the constrained limits shown in Table 3. Alternatively, we can marginalize over the possible directions of the dipole, which will necessarily result in weaker limits than when the direction is fixed. This is particularly true here, where the direction of greatest uncertainty in the dipole measurement is roughly orthogonal to the

expected dipole direction. In the case of the Compton-Getting dipole, there is a strong prior that it should be in the CMB dipole direction, so our limit is stronger than it would be if we did not have information about the CMB.

In addition to the upper limit on the intrinsic dipole amplitude, we can also constrain the underlying dipole variance, which can, in turn, be used to test theoretically predicted power spectra. While the observed amplitude is related to the dipole variance, $\langle \Delta^2 \rangle = 3\sigma_{\Delta}^2$, there is large uncertainty due to cosmic variance. The dipole represents only three independent samplings of σ_{Δ} . To constrain σ_{Δ} , we again take a Bayesian approach and calculate the likelihood of observing the data given the noise and σ_{Δ} ,

$$\mathcal{P}(\Delta|\sigma_{\Delta}) \propto \prod e^{-\Delta_i^2/2(\sigma_i^2 + \sigma_{\Delta}^2)} (\sigma_i^2 + \sigma_{\Delta}^2)^{-1/2}, \quad (6)$$

where the product is over the three spatial directions and we have ignored the small off-diagonal noise correlations (see Table 2). With a uniform prior on σ_{Δ} , its posterior distribution implies a 95% CL upper limit of $\sigma_{\Delta} < 0.0064$. This is twice as high as would be inferred from the limit on the dipole because of the significant tail in the distribution due to cosmic variance. The limit implied by the dipole (of map C), $\sigma_{\Delta} = \Delta/\sqrt{3} < 0.0030$, is at the 80% CL. The difference between the limits arises because occasionally a small dipole can occur even when the variance is large.

The bottom line is that we have detected the dipole in the XRB at about the 2σ level and that it is consistent with the Compton-Getting dipole. There is no evidence for any other intrinsic dipole at this same level. We will discuss the apparent detection of an intrinsic dipole by Scharf et al. (2000) in § 6.

5. CORRELATIONS IN THE X-RAY BACKGROUND

A standard way to detect the clustering of sources (or of the emission of these sources) is to compute the autocorrelation function (ACF), defined by

$$\omega(\theta) = \frac{1}{\bar{I}^2 N_{\theta}} \sum_{i,j} (I_i - \bar{I})(I_j - \bar{I}), \quad (7)$$

where the sum is over all pairs of pixels, i, j , separated by an angle θ , I_i is the intensity of the i^{th} pixel, \bar{I} is the mean intensity, and N_{θ} is the number of pairs of pixels separated by θ . Figure 3 shows the ACF of the residual map after being corrected with the eight-parameter fit and for photon shot noise in the $\theta = 0^{\circ}$ bin. The error bars are highly correlated and were determined from Monte Carlo trials in which the pixel intensity distribution was assumed to be Gaussian with the same ACF as in the figure. There is essentially no significant structure for $\theta > 13^{\circ}$ once local structures have been removed, as is evident in Figures 3, 4, and 5.

It is clear from Figure 3 that the residuals of map A possess significant correlated structure. It must be determined how much, if any, is due to clustering in the XRB and how much is simply due to smearing by the PSF of the map. It is straightforward to show that an uncorrelated signal smeared by a Gaussian PSF, $\text{PSF}(\theta) \propto e^{-\theta^2/2\sigma_p^2}$, results in an ACF of the form $\omega(\theta) \propto e^{-\theta^2/4\sigma_p^2}$, where $\sigma_p = 1.29$ is the Gaussian width of the PSF in Figure 2 ($\theta_{\text{FWHM}}^2 = 8\sigma_p^2 \ln 2$.) The dashed curve in Figure 3 is essentially this functional form, modified slightly to take into account the pixelization. In the plot, its amplitude has been forced to agree with the

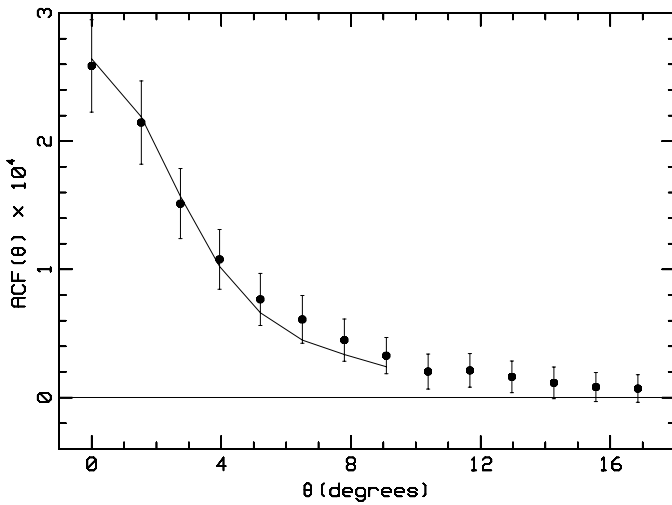


FIG. 5.—Intrinsic ACF, with shot noise and PSF fits removed. For comparison, a simple θ^{-1} model for the intrinsic correlations is shown. The data beyond 9° is not used because of uncertainty due to the fitting of the large-scale structures. The model has been smoothed by the PSF and corrected for the removal of the large-scale structures, which suppresses the correlations on scales larger than 10° .

$\theta = 0^\circ$ data point, while a maximum likelihood fit results in an amplitude about 5% lower (a consequence of the correlated noise). For $\theta \gtrsim 3^\circ$, the ACF of the data clearly exceeds that explainable by beam smearing, and this excess is even more pronounced with the maximum likelihood fit. The reduced χ^2 for the fit to the first eight data points ($\theta \lesssim 9^\circ$) is $\chi^2 = 18.6$ for 6 degrees of freedom, which is another measure of the excess structure between 3° and 9° . Note, this is a two-parameter fit since the photon shot noise (which occurs only at $\theta = 0^\circ$) is also one of the parameters.

While it is apparent that there is some intrinsic correlation in the XRB, it cannot be estimated by the residual to the above two-parameter fit since that overestimates the contribution of beam smearing in order to minimize χ^2 . Instead, we also include in the fit a form for the intrinsic correlation and find its amplitude as well. Since the signal-to-noise ratio is too small to allow a detailed model of the intrinsic clustering, we chose to model it with a simple power law $\omega(\theta) = (\theta_0/\theta)^\epsilon$. This form provides an acceptable fit to the ACF of both radio and X-ray surveys on somewhat smaller angular scales (Cress & Kamionkowski 1998; Soltan et al. 1996; Giacconi et al. 2001). This intrinsic correlation was then convolved with the PSF and applied to the quad cube pixelization of the map (e.g., Boughn 1998).

Finally, it is important to take into account the effects of the eight-parameter fit used to remove the large-scale structure as discussed in § 3. If the XRB has intrinsic structure on the scale of many degrees, the eight-parameter fit will tend to remove it in order to minimize χ^2 . Since the model is composed of relatively large scale features, the greatest effect is expected for the largest angles. The significance of this effect was determined by generating Monte Carlo trials assuming a Gaussian pixel intensity distribution with the same ACF as in Figure 3. The eight-parameter model was then fitted, and each trial map was corrected accordingly. The ACFs computed for these corrected maps indicate that, as expected, the value of the ACF is significantly attenuated for larger angles. The attenuation factor for $\theta = 9^\circ$ is already 0.55 and decreases rapidly for larger angles. The

errors indicated in Figure 3 were also determined from these Monte Carlo trials and, as mentioned above, are highly correlated.

We model the autocorrelation function as a sum of three templates and fit for their best amplitude. Much of the analysis parallels the discussion for the fits of large-scale structure in the map, with the exception that here the number of bins is small enough that it is simple to calculate the maximum likelihood fit. Again, we model the observed correlation function vector as $\omega = \tilde{W}\mathbf{c} + \mathbf{n}_\omega$, where \tilde{W} is a $3 \times n_{\text{bin}}$ matrix containing the templates for shot noise (ω_s), beam smearing (ω_{PSF}), and intrinsic correlations in the XRB (ω_{intr}). The amplitudes are given by the three-element vector \mathbf{c} , and the noise is described by the correlation matrix determined from Monte Carlo trials, $\tilde{C}_\omega = \langle \mathbf{n}_\omega \mathbf{n}_\omega^T \rangle$.

Shot noise contributes only to the first bin (zero separation) of the ACF and has amplitude given by its variance, ω_s . Beam smearing contributes to the ACF with a template that looks like the beam convolved with itself, so appears as a Gaussian with an FWHM a factor of $\sqrt{2}$ larger than that of the beam and has amplitude denoted as ω_{PSF} . Finally, the intrinsic correlations are modeled as $(\theta_0/\theta)^\epsilon$, which is then smoothed appropriately by the beam. Its amplitude is denoted by its inferred correlation at zero separation, ω_{intr} . We fit using a range of indices, $0.8 \geq \epsilon \geq 1.6$, which cover the range of theoretical models of the intrinsic correlation. Both the PSF template and the intrinsic template are modified to include the effects of the attenuation at large angles as discussed above.

Minimizing χ^2 with respect to the three fit parameters, \mathbf{c} , results in the maximum likelihood fit to the model if one assumes Gaussian statistics. This assumption is reasonable by virtue of the central limit theorem since each data point consists of the combination of the signals from a great many pixels, each of which is approximately Gaussian distributed. In the presence of correlated noise, χ^2 is defined by

$$\chi^2 = (\omega - \tilde{W}\mathbf{c})^T \tilde{C}_\omega^{-1} (\omega - \tilde{W}\mathbf{c}). \quad (8)$$

It is straightforward to show that the value of the parameters that minimize χ^2 are given by

$$\mathbf{c} = \Omega^{-1} \tilde{W}^T \tilde{C}_\omega^{-1} \omega, \quad (9)$$

where $\Omega = \tilde{W}^T \tilde{C}_\omega^{-1} \tilde{W}$. Because of the large attenuation of the ACF at large angles, we chose to fit to only those data points with $\theta_i \leq 9^\circ$, i.e., $i \leq 8$, even though there appears to be statistically significant structure out to $\theta \sim 13^\circ$. The results of the fit of the $\epsilon = 1$ model to the ACF of the residuals of map A are listed in Table 4 and plotted in Figure 3.

It is also straightforward to show that the correlation matrix of the fit parameters is given by $\langle \delta c_n \delta c_m \rangle = \Omega_{nm}^{-1}$, so the errors given in Table 4 are given by $\sigma_{c_n}^2 = \Omega_{nn}^{-1}$ and the normalized correlation coefficients by $r_{nm} = \Omega_{nm}^{-1} / (\Omega_{nn}^{-1} \Omega_{mm}^{-1})^{1/2}$. The correlations are as expected; i.e., ω_{intr} and ω_{PSF} are highly correlated, while ω_s is relatively uncorrelated with the other two parameters.

From the results in Table 4 it appears that intrinsic correlations in the XRB are detected at the 4σ level for sources with flux levels below 3×10^{-11} ergs $\text{s}^{-1} \text{cm}^{-2}$. Of course, if we have not successfully eliminated sources with fluxes larger than this, then the clustering amplitude might well be artificially inflated. It was for this reason that we used the RASS catalog to identify and remove additional sources

TABLE 4
FIT MODEL PARAMETERS FOR MAP A WITH 55% SKY COVERAGE AND MAP B WITH 52% SKY COVERAGE
AFTER REMOVING ADDITIONAL *ROSAT* SOURCES (SEE § 2)

Map	$\omega_s \times 10^4$	$\omega_{\text{PSF}} \times 10^4$	$\omega_{\text{intr}} \times 10^4$	χ^2_5	r_{12}	r_{13}	r_{23}
A.....	7.71 ± 0.15	8.63 ± 0.59	2.64 ± 0.65	2.3/5	-0.19	-0.04	-0.83
B.....	7.57 ± 0.15	8.22 ± 0.59	2.33 ± 0.65	3.6/5	-0.19	-0.04	-0.83

NOTE.—The intrinsic fluctuations are modeled as $\omega \propto \theta^{-1}$.

with intensities $\gtrsim 3 \times 10^{-11}$ ergs s $^{-1}$ cm $^{-2}$, the result of which was map B (see § 2). The fits to map B are also listed in Table 4. The clustering amplitude, ω_{intr} , of the fits to this modified map was only 11% less than that of map A, i.e., considerably less than 1 σ . The χ^2 of both fits are acceptable.

These results are not very sensitive to the attenuation corrections. If they are removed from the model, the resulting amplitude of the fit clustering coefficient decreases by only $\sim 20\%$, less than 1 σ . It should be noted that the corrections were relatively small (an average attenuation factor of 0.83 ranging from 1.0 at $\theta = 0^\circ$ to 0.55 for $\theta = 9^\circ$) and in all cases, the attenuation was less than the error bar of the corresponding data point. If data points with $\theta > 9^\circ$ are included, the fits become more sensitive to the attenuation corrections, which are, in turn, quite sensitive to the eight-parameter fit.

Figure 4 is a plot of the residuals of the fit to the ACF of map A for $\theta \leq 9^\circ$ and of the uncorrected ACF from 10° to 180° . The vertical scale is the same as for Figure 3. The rms of these 140 data points is 1×10^{-5} , and it is clear that there is very little residual structure at levels exceeding this value. The observed correlation function for $\theta > 10^\circ$ in Figure 4 is entirely consistent with the noise levels determined from the Monte Carlo simulations: the rms of ω/σ is 1.03, indicating that there is no evidence for intrinsic fluctuations on these scales. We also take this as an indication that the errors are reasonably well characterized by the Monte Carlo calculation. The variance of the photon shot noise, $\sigma_s^2 = \omega_s \bar{I}^2$, is consistent with that expected from photon counting statistics only (K. Jahoda 2001, private communication). It should be noted that not only the shape but the amplitude of the beam-smearing contribution, ω_{PSF} , can be computed from source counts as a function of 2–10 keV flux. We will argue in § 6 that, while our fitted value is consistent with current number counts, the latter are not yet accurate enough to correct the data.

Figure 5 shows the model of the intrinsic clustering, ω_{intr} , compared to the data with both the shot noise and PSF component removed. The model curve is not plotted beyond $\theta = 9^\circ$ since the attenuation factor due to the eight-parameter fit corrections is large and uncertain at larger angles. The amplitude of ω_{intr} is sensitive to the exponent in the assumed power law for the intrinsic correlations. For example, the fit amplitude for a $\theta^{-1.6}$ power law is a factor of ~ 2 larger than for a $\theta^{-0.8}$ power law. However, for a range of fits with $0.8 \leq \epsilon \leq 1.6$, the values of $\omega_{\text{intr}}(\theta)$ at $\theta = 4.5$ are all within $\pm 3\%$ of each other. Therefore, we chose to normalize the X-ray ACF at 4.5 when comparing to cosmological models (see § 7.1). The χ^2 are reasonable for all these fits.

The bottom line is that there is fairly strong evidence for intrinsic clustering on these angular scales at the level of $\omega_{\text{XRB}} \sim 3.6 \times 10^{-4} \theta^{-1}$ (see § 6.1). While the exponent is

$\epsilon \sim 1$, it is not strongly constrained. The implications of the intrinsic clustering of the XRB will be discussed in § 7.

6. COMPARISONS WITH PREVIOUS WORK

6.1. Clustering

As mentioned above, the component of the ACF due to beam smearing, ω_{PSF} , can be determined with no free parameters if the flux-limited number counts of X-ray sources are known. While such counts are still relatively inaccurate for our purposes, we did check to see whether our results are consistent with current data. Over a restricted flux range, the X-ray number counts, $N(<S)$, are reasonably approximated by a power law, i.e., $N(<S) = KS^{-\gamma}$, where S is the flux of the source. It is straightforward to show that the variance of flux due to a Poisson distribution of sources is

$$\sigma_{\text{PSF}}^2(0) = \frac{\pi \sigma_p^2 A^2 \gamma K S^{2-\gamma}}{2 - \gamma}, \quad (10)$$

where S is the upper limit of source flux, σ_p is the Gaussian width of the PSF, and A^{-1} is the flux of a point source that results in a peak signal of 1 TOT counts s $^{-1}$ in our composite map. In our case, $A = 2.05 \times 10^{10}$ ergs $^{-1}$ s cm 2 . Using the *BeppoSAX* 2–10 keV number count data of Giommi, Perri, & Fiore (2000), the *Chandra* data of Mushotzky et al. (2000), and the *HEAO 1* A-2 data of Piccinotti et al. (1982), we constructed a piecewise power law $N(<S)$ for the range 6×10^{-16} ergs s $^{-1}$ cm $^{-2} < S < 3 \times 10^{-11}$ ergs s $^{-1}$ cm $^{-2}$ and computed $\omega_{\text{PSF}}(0) = \sigma_{\text{PSF}}^2 / \bar{I}^2$ to be 8.4×10^{-4} . The close agreement of this value with those in Table 4 is fortuitous given that the value depends most sensitively on the number counts at large fluxes, which are the most unreliable, typically accurate only to within a factor of 2. However, it is clear that the ω_{PSF} of Table 4 are quite consistent with the existing number count data.

The results of § 5 clearly indicate the presence of intrinsic clustering in the XRB. Mindful that the detection is only $\sim 4 \sigma$, we tentatively assume that the ACF has an amplitude of $\omega_{\text{intr}} \sim 2.5 \times 10^{-4}$ (the average of the two values in Table 4) and is consistent with a θ^{-1} functional dependence. It is straightforward to relate this to the underlying correlation amplitude, θ_0 . The variance of correlations smoothed by a beam of Gaussian size σ is given by

$$\omega_{\text{intr}}(0) = \frac{\Gamma(1 - \epsilon/2)}{2^\epsilon} \left(\frac{\theta_0}{\sigma} \right)^\epsilon. \quad (11)$$

When $\epsilon = 1$, then $\theta_0 = 2\sigma\omega_{\text{intr}}/\pi^{1/2}$. Using this, we find

$$\omega_{\text{XRB}}(\theta) \simeq 3.6 \times 10^{-4} \theta^{-1}, \quad (12)$$

where θ is measured in degrees and the normalization is such that $\omega_{\text{XRB}}(0) = \langle \delta I^2 \rangle / \bar{I}^2$.

For comparison, this amplitude is about a factor of 3 below the 2σ upper limit determined by Carrera et al. (1993) obtained with *Ginga* data (4–12 keV) for angular scales between $0^\circ 2$ and $2^\circ 0$. The detection of a significant correlation in the *HEAO 1* A-2 data at the level of 3×10^{-5} at $\theta = 10^\circ$ by Mushotzky & Jahoda (1992) was later attributed to structure near the super-Galactic plane (Jahoda 1993). To check for this effect in the present analysis, we masked all pixels within 15° and 20° from the super-Galactic plane. The results were indistinguishable from those of Table 4. It is interesting that the clustering indicated in equation (12) is consistent with this level of fluctuations at 10° ; however, our sensitivity has begun to decline significantly at 10° because of the fit for large-scale structures. A correlation analysis of *ROSAT* soft X-ray background by Soltan et al. (1996) detected correlations about 1 order of magnitude larger than indicated in equation (12). Even considering that the *ROSAT* band (0.5–2.0 keV) is distinct from the *HEAO* band, it is difficult to imagine that the two correlation functions could be so disparate unless the lower energy analysis is contaminated by the Galaxy.

While there has yet to be a definitive detection of the clustering of hard X-ray sources, a recent deep *Chandra* survey of 159 sources shows a positive correlation of source number counts on angular scales of $5''$ – $100''$ (Giacconi et al. 2001). Although the signal-to-noise ratio is low and dependent on source flux, the implied number count ACF is roughly consistent with $\omega_N(\theta) \sim 3 \times 10^{-3} \theta^{-1}$, where $\omega_N(0) \equiv \langle \delta N^2 \rangle / \bar{N}^2$ and \bar{N} is the mean surface density of sources. This is consistent with the correlation function determined by Vikhlinin & Forman (1995) for sources identified within *ROSAT* PSPC deep pointings. A direct comparison between the *Chandra* result and that of equation (12) is complicated by the more than 100 times difference in the angular scales of the two analyses. It is doubtful that a single power-law model is adequate over this range. Furthermore, one is a luminosity ACF, while the other is a flux-limited, number count ACF. Relating the two requires understanding the luminosity function and its evolution as well as how the X-ray bias depends on scale. For these reasons, a direct comparison would be difficult to interpret. We only note in passing that the small angular scale ACF is a factor of 8 larger than that of equation (12) assuming a θ^{-1} dependence.

Finally, the recent harmonic analysis of the *HEAO 1* A-2 data by Scharf et al. (2000) yielded a positive detection of structure in the XRB out to harmonic order $l \sim 10$. The present analysis looks at similar maps, so the results should be comparable. A direct comparison is complicated by the differences in analysis techniques, masking, and corrections to the map. A rough comparison can be made by performing a Legendre transform on the θ^{-1} ACF model of equation (12). The ACF can be expressed in terms of Legendre polynomials as

$$\omega(\theta) = \frac{1}{4\pi} \sum_{\ell} (2\ell + 1) C_{\ell} P_{\ell}(\cos \theta), \quad (13)$$

where the C_{ℓ} constitute the angular power spectrum. Taking

the Legendre transform

$$C_{\ell} = 2\pi \int_{-1}^1 \omega(\theta) P_{\ell}(\cos \theta) d(\cos \theta), \quad (14)$$

where $P_{\ell}(\theta)$ is the Legendre polynomial of order ℓ . Substituting the θ^{-1} model into this expression results in power spectrum coefficients, $C_{\ell} \simeq 4 \times 10^{-5} / \ell$ for $\ell \sim 5$. Note that for $\ell \sim 5$, this expression is relatively insensitive to the index ϵ in the expression for ω_{intr} . While these values are highly uncertain, they are comparable to those found by Scharf et al. (2000) when the sky coverage and differences in notation are accounted for. Considering the low signal-to-noise ratio of the data as well as the differences in the two analyses, a more detailed comparison would not be particularly useful.

6.2. The Dipole

Scharf et al. (2000) also searched for the XRB dipole using a *HEAO 1* A-2 map and similar methods to those described in § 4. They claim a detection of an intrinsic dipole with amplitude $\Delta \sim 0.0065$, though with a rather large region of uncertainty, i.e., $0.0023 \lesssim \Delta \lesssim 0.0085$, and in a direction about 80° from that of the Compton-Getting dipole, in the general direction of the Galactic center. They used the $3^\circ \times 1^\circ 5$ *HEAO 1* A-2 map restricted to regions farther than 22° from the Galactic plane. In addition, regions about sources with fluxes greater than 2×10^{-11} ergs $\text{s}^{-1} \text{cm}^{-2}$ were cut from the map. The sky coverage and the level of source removal closely correspond to those of our map C. However, since we used a combination of the $3^\circ \times 1^\circ 5$ and $3^\circ \times 3^\circ$ maps, our map has significantly less ($\sim 1/\sqrt{3}$) photon shot noise. While our analyses are similar, there are some significant differences: they corrected the map beforehand for linear instrument drift and Galaxy emission, while we fit for those components simultaneously with the dipole and with emission from the Local Supercluster, which they ignore.

The upper limit on the intrinsic dipole we find is about the same amplitude as the Compton-Getting dipole, i.e., $\Delta < 0.0052$ at the 95% CL. Thus, we exclude roughly the upper half of the Scharf et al. range and believe that their claim of a detection is probably an overstatement. While Scharf et al. do not take into account emission from the plane of the Local Supercluster, even if we leave that component out of our fit, the dipole moment (including the C-G dipole) increases by only 0.005 TOT counts s^{-1} and is still consistent with the C-G dipole. The upper limit on the intrinsic dipole with this fit is determined primarily by the noise in the fit and is not significantly different from that value given above. It is difficult to understand how their quoted errors could be 2–4 times less than those quoted in Table 3. The shot-noise variance in the map they used was 3 times greater than in our combination map, so one would expect their errors to be somewhat larger than those above. They performed only a four-parameter fit (offset plus dipole), which would result in a slight reduction of error; however, this is a bit misleading since their Galaxy model and linear time drift are derived from essentially the same data set. It is possible that their lower errors could result from ignoring correlations in the noise (our detected ACF). In any case, we find no evidence for an intrinsic dipole moment in the XRB.

7. IMPLICATIONS FOR COSMOLOGY

7.1. Clustering and Bias in the X-Ray Background

The observed X-ray autocorrelation can be compared to the matter autocorrelation predicted by a given cosmological model. The linear bias factor for the X-rays can then be determined by normalizing to the observed CMB anisotropies. Since X-rays arise at such high redshifts, the fluctuations we measure are on scales $\lambda \sim 100 h^{-1}$ Mpc, comparable to those constrained by the CMB, i.e., on wavelengths that entered the horizon about the time of matter domination.

The predicted X-ray ACF depends both on the cosmological model and on the model for how the X-ray sources are distributed in redshift, which is constrained by observed number counts and the redshift measurements of discrete sources. We use the redshift distribution described in Boughn, Crittenden, & Turok (1998), based on the unified AGN model of Comastri et al. (1995). (See also the more recent analysis by Gilli, Salvati, & Hasinger 2001.) While we will not reproduce those calculations here, the basic result is that the XRB intensity is thought to arise fairly uniformly in redshift out to $z = 4$. Our results here are not very sensitive to the precise details of this distribution.

Another issue in the calculation of the power spectrum is the possible time dependence of the linear bias. Some recent studies indicate that the bias is tied to the growth of fluctuations and may have been higher at large redshift (Fry 1996; Tegmark & Peebles 1998). For the purposes of the power spectrum, an evolving bias will have the same effect as changing the source redshift distribution. Again, our results are not strongly dependent on these uncertainties, but they comprise an important challenge to using the X-ray fluctuation studies to make precision tests of cosmology.

Figure 6 shows the predicted XRB power spectrum, normalized to our observations. On the scales of interest, the predicted spectra are fairly featureless and reasonably described by a power law in ℓ , $C_\ell \propto \ell^{\epsilon-2}$, which corresponds to the correlation of the form $\omega(\theta) = (\theta_0/\theta)^\epsilon$. For the models of interest, $1.1 < \epsilon < 1.6$ for $\ell < 100$ and decreases at higher ℓ (smaller separations). Note that the spectra calculated by Treyer et al. (1998) appear to be consistent with our findings, suggesting $\epsilon = 1.2$. The precise index ϵ depends on the position of the power spectrum peak, which is determined by the shape parameter, $\Gamma \simeq \Omega_m h$. Larger values of Γ imply more small-scale power and thus higher ϵ .

For simplicity, we normalize to the X-ray correlation function at $4^\circ.5$, $\omega(4^\circ.5) = 1.0 \pm 0.25 \times 10^{-4}$. This separation is large enough to be independent of the PSF contribution to the ACF but not so large that the attenuation from the large-scale fits becomes significant. In addition, the value of the fit ACF at $4^\circ.5$ is nearly independent of the index ϵ (see § 5). As can be seen from Figure 6, this normalization fixes the power spectrum at $\ell \simeq 5-7$.

We normalize the fluctuations to the *COBE* power spectrum as determined by Bond, Jaffe, & Knox (1998). However, it should be noted that fits to smaller angular CMB fluctuations indicate that using *COBE* alone may somewhat overestimate the matter fluctuation level (Lahav et al. 2002). The biases derived from the models appear to be largely insensitive to the matter density. This is due to a cancellation of two effects: the CMB normalization and the power spectrum shape (White & Bunn 1995). The biases are roughly inversely proportional to h . Typical biases appear

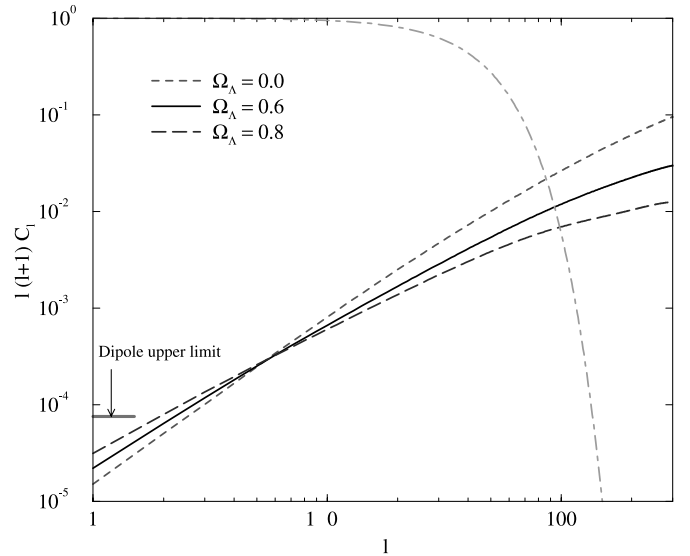


FIG. 6.—Power spectrum for a range of cosmologies normalized to the observations ($H_0 = 70 \text{ km s}^{-1} \text{ Mpc}^{-1}$). The various cosmologies show a range of slopes $1.1 < \epsilon < 1.6$, and the observations fix them at $\ell \simeq 5$. Also shown is the 95% upper limit from the dipole, excluding cosmic variance. With cosmic variance, the limit shown is at the 80% confidence level, and the 95% upper limit is 4 times higher. The dot-dashed line shows the suppression arising from beam smoothing, which smooths scales $\ell > 50$. [See the electronic edition of the *Journal* for a color version of this figure.]

to be $b_X = 2.3 \pm 0.3(0.7/h)^{0.9}$, increasing slightly as Γ decreases and the peak of the power spectrum moves to larger scales.

7.2. The Intrinsic X-Ray Dipole

The theoretical models normalized to our observations predict the intrinsic power on a wide range of scales, assuming the X-ray bias is scale independent. In particular, these models give a prediction for the variance of the intrinsic dipole moment. We can compare our model predictions to the upper limit for the intrinsic dipole to see if we should have observed it in the X-ray map.

The dipole amplitude in the \hat{z} -direction is related to the spherical harmonic amplitude by $\Delta_z = (3/4\pi)^{1/2} a_{10}$. Thus, the expected dipole amplitude is related to the power spectrum by

$$\langle \Delta^2 \rangle = 3 \times \frac{3}{4\pi} \langle |a_{1m}|^2 \rangle = \frac{9}{4\pi} C_1. \quad (15)$$

Note that there is considerable cosmic variance on this because it is estimated with only three independent numbers; $\delta C_1/C_1 = (\frac{2}{3})^{1/2}$, which corresponds to a 40% uncertainty in the amplitude of the dipole.

Also shown in Figure 6 is the level of our dipole limit, translated using equation (15), which corresponds to $C_1 < 3.8 \times 10^{-5}$. While our limit on the dipole limit is at the 95% CL, this translates to an 80% CL limit on the variance C_1 when cosmic variance is included. As discussed above, the 95% upper limit is 4 times weaker when cosmic variance is included, $C_1 < 1.5 \times 10^{-4}$. Normalized to the ACF, all the theories are easily compatible with the C_1 bound. The large cosmic variance associated with the dipole makes it difficult to rule out any cosmological models.

With our detected level of clustering, typical theories would predict a dipole amplitude of $\Delta \simeq 0.003$. While the

theories are not in conflict with the dipole range claimed by Scharf et al., they strongly prefer the lower end of their range, even for the most shallow of the models. A dipole amplitude $\Delta \geq 0.005$ would be very unlikely from the models, indicating either a significantly higher bias than we find or a model with more large-scale power ($\epsilon \leq 1.1$).

7.3. The Dipole and Bulk Motions

The dipole of the XRB provides another independent test of the large-scale X-ray bias through its relation to our peculiar velocity (e.g., see Scharf et al. 2000 and references therein.) Like the gravitational force, the flux of a nearby source drops off as an inverse-square law, so the dipole in the X-ray flux is proportional to the X-ray bias times the gravitational force produced by nearby matter. Our peculiar motion is a result of this force and is related to the gravitational acceleration by a factor that depends on the matter density.

In typical CDM cosmologies, the dipole and our peculiar velocity arise because of matter at fairly low redshifts ($z < 0.1$). If this is the case, it is straightforward to relate their amplitudes. Following the notation of Scharf et al., we define $D^\alpha = \int d\Omega I(\hat{n}) \hat{n}^\alpha = 4\pi \bar{I} \Delta^\alpha / 3$. Using linear perturbation theory, one can show that the local bulk flow is

$$v^\alpha = \frac{H_0 f}{b_X(0) \rho_X(0)} D^\alpha, \quad (16)$$

where $\rho_X(0)$ is the local X-ray luminosity density, $b_X(0)$ is the local X-ray bias, and $f \simeq \Omega_m^{0.6}$ is related to the growth of linear perturbations (Peebles 1993). From the mean observed intensity (Gendreau et al. 1995) and the local X-ray luminosity density (Miyaji et al. 1994) we find that $\bar{I} \simeq 2.4 \rho_X(0) c / 4\pi H_0$. This implies that

$$|v| \simeq 2.4 \times 10^5 \Delta \frac{\Omega_m^{0.6}}{b_X(0)} \text{ km s}^{-1}. \quad (17)$$

This relation was derived by Scharf et al. (2000), although their numerical factor was computed from a fiducial model rather than directly from the observations, as above. In any case, the uncertainty in $\rho_X(0)$ is considerable, $6 \times 10^{38} \text{ ergs s}^{-1} \text{ Mpc}^{-3} < \rho_X(0) < 15 \times 10^{38} \text{ ergs s}^{-1} \text{ Mpc}^{-3}$ (Miyaji et al. 1994), and so is the uncertainty in this relation.

Our maps have bright sources removed, which correspond to nearby sources out to $60 h^{-1} \text{ Mpc}$. Thus, we need to compare our dipole limit to the motion of a sphere of this radius centered on us. Typical velocity measurements on this scale find a bulk velocity of $v_{60} \simeq 300 \pm 100 \text{ km s}^{-1}$ (see Scharf et al. 2000 for a summary). With our dipole limit, this implies that $\Omega_m^{0.6} / b_X(0) \gtrsim 0.24 \pm 0.08$ where the uncertainty in $I / \rho_X(0)$ is not included. This constraint is independent of cosmic variance issues. While the diameter of the Local (Virgo) Supercluster is generally considered to be on the order of $40 h^{-1}$ to $50 h^{-1} \text{ Mpc}$ (e.g., Davis et al. 1980), there is evidence that the overdensity in the super-Galactic plane extends significantly beyond $60 h^{-1} \text{ Mpc}$ (Lahav et al. 2000). One might, therefore, suspect that our correction for emission from the Local Supercluster might effectively remove sources at distances greater than $60 h^{-1} \text{ Mpc}$ in that plane. In any case, that correction made very little difference in dipole fits (see § 6.2), so our conclusions remain the same.

Note that this limit could potentially conflict with previous determinations by Miyaji (1994), who found $\Omega_m^{0.6} / b_X(0) = f_{45} / 3.5$, where f_{45} is the fraction of gravitational acceleration arising from $R \leq 45 h^{-1} \text{ Mpc}$. This is consistent only for $f_{45} \sim 1$, which is larger than is usually assumed ($f_{45} \sim 0.5$). However, this limit comes from studies of a fairly small sample (16) of X-ray-selected AGNs and is subject to significant uncertainties of its own.

For typical biases suggested by the observed clustering ($b_X \sim 2.3$), our constraint suggests a somewhat high matter density, $\Omega_m > 0.37$, for $v_{60} \simeq 300 \text{ km s}^{-1}$. This is consistent with the ISW constraint discussed below and also with previous analyses of bulk velocities, which tend to indicate higher Ω_m . However, if the bulk velocity is smaller and/or $\rho_X(0)$ larger, this constraint is weakened. In addition, we have assumed a constant X-ray bias. If the bias evolves with redshift, then the local value could be considerably smaller, which would also weaken this bound.

7.4. The Integrated Sachs-Wolfe Effect and Ω_Λ

In models where the matter density is less than unity, microwave background fluctuations are created very recently by the evolution of the linear gravitational potential. This is known as the late-time integrated Sachs-Wolfe (ISW) effect. Photons gain energy as they fall into a potential well and lose a similar amount of energy as they exit. However, if the potential evolves significantly as the photon passes through, the energy of the photons will be changed, leaving an imprint on the CMB sky. The spectrum is modified most on large scales where the photons receive the largest changes.

The CMB anisotropies created in this way are naturally correlated with the gravitational potential. Thus, we expect to see correlations between the CMB and tracers of the local ($z \sim 2$) gravitational potential such as the XRB (Crittenden & Turok 1996). These correlations are primarily on large scales such as those probed by the *HEAO* survey.

In an earlier paper, we searched for a correlation between the *HEAO* maps and maps of the CMB sky produced by *COBE*. We failed to find such a cross-correlation and were able to use our limit to constrain the matter density and the X-ray bias (Boughn, Crittenden, & Turok 1998, hereafter BCT). However, translating our measurement into a cosmological bound was ambiguous because the level of the intrinsic structure of the XRB was unknown at the time. With the observation of the X-ray ACF presented here, we are in a position to revisit the cosmological limits implied by these measurements.

To make cosmological constraints, we compare the observed X-ray/CMB cross-correlation to those predicted by Λ CDM models. As above, we normalize the CMB fluctuations using the band powers of *COBE* (Bond et al. 1998) and also normalize the X-ray fluctuations as discussed in § 7.1. The cross-correlation analysis of BCT was performed with a coarser pixelization (2.6×2.6) than the ACF discussed above. We include this effect by using the numerically calculated pixelization window function. The *COBE* PSF used was that found by Kneissl & Smoot (1993), and we used a 2.9 FWHM Gaussian for the underlying X-ray PSF (recall that the 3.04 FWHM beam found above includes a 1.3×1.3 pixelization.)

The calculation of the *HEAO-COBE* cross-correlation was discussed in BCT and has not changed. The results are

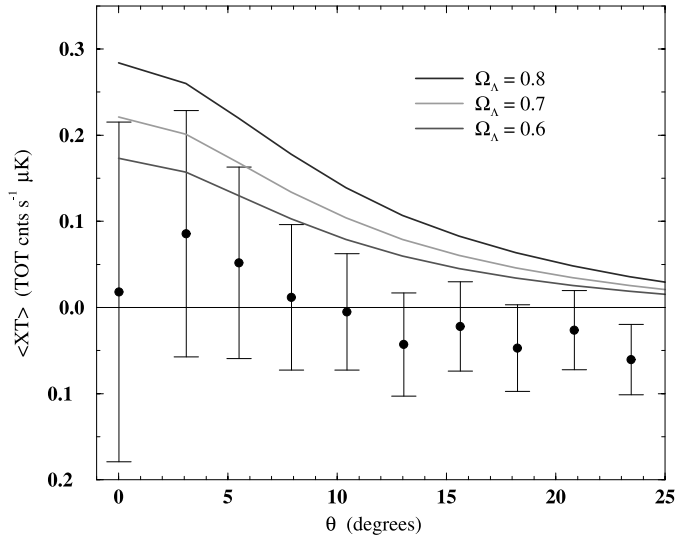


FIG. 7.—Calculated X-ray/CMB cross-correlation. The error bars are highly correlated. Also shown are the predictions for three Λ CDM models with varying Ω_Λ ($H_0 = 70 \text{ km s}^{-1} \text{ Mpc}^{-1}$). [See the electronic edition of the *Journal* for a color version of this figure.]

shown in Figure 7, along with predictions for three different values of Ω_Λ . While the X-ray bias depends strongly on the Hubble parameter, the predicted cross-correlation is only weakly dependent on it, changing only 10% for reasonable values of H_0 . The cross-correlation depends primarily on Ω_Λ ; no correlation is expected if there is no cosmological constant and the ISW effect increases as Ω_Λ grows. The error bars in Figure 7 are calculated from Monte Carlo simulations and arise primarily because of cosmic variance in the observed correlation. The error bars are significantly correlated.

The observed correlation is most consistent with there being no intrinsic cross-correlation ($\Omega_\Lambda = 0.0$). We set limits by calculating the likelihood of a model relative to this no-correlation model. Using the frequentist criterion used in BCT, $\Omega_\Lambda \leq 0.65$ at the 98% CL, $\Omega_\Lambda \leq 0.60$ at the 95% CL. Almost identical limits arise from a Bayesian approach, where the relative likelihoods are marginalized over, assuming a constant prior for $\Omega_\Lambda \geq 0$. Figure 8 shows a one-dimensional slice through the likelihood surface, where only the cross-correlation information has been used to calculate the likelihood.

One of the major assumptions we made in interpreting the above result is how the sources of the XRB are distributed in redshift. It is likely that current models of the luminosity function will have to be substantially modified as further deep observations of the sources of the XRB are made. However, as pointed out above, the ISW is relatively insensitive to the exact shape of the redshift distribution of luminosity. If the true distribution includes a substantial fraction of the luminosity at redshifts greater than 1, then the above results will not change dramatically. On the other hand, our constraint on Ω_Λ is quite sensitive to the value of the bias parameter. If the sources of the XRB should turn out to be unbiased, i.e., $b_X = 1$, then the constraint on Ω_Λ could be weakened dramatically. We hasten to add that such a low bias would require that the ACF of Figure 5 be reduced by more than a factor of 4, which seems unlikely. Previous determinations of X-ray bias have resulted in a wide range of values, $1 < b_X < 7$ (see Barcons et al. 2001

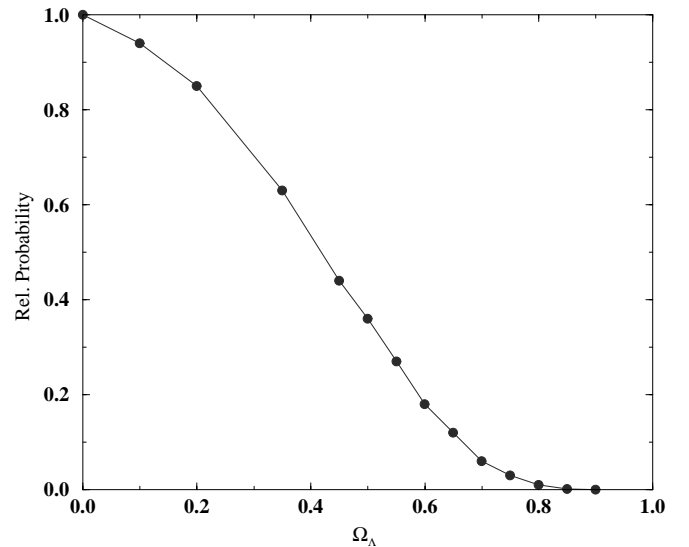


FIG. 8.—Relative probability of the observed cross-correlation for varying cosmological constant, with the Hubble constant fixed ($H_0 = 70 \text{ km s}^{-1} \text{ Mpc}^{-1}$). The best fit is for no correlation. [See the electronic edition of the *Journal* for a color version of this figure.]

and references therein). It is clear that firming up the value of b_X and determining how it varies with scale and redshift will be required before the ISW effect can be unambiguously interpreted.

The above limit may be compared to what we found from cross-correlating *COBE* with the NRAO VLA Sky Survey galaxy survey (Boughn & Crittenden 2002). There we also found no evidence for correlations and were able to put a 95% CL limit of $\Omega_\Lambda \leq 0.74$, with some weak dependence on the Hubble constant. While the above limit provides important confirmation of that result, it should be noted that these two limits are not entirely independent. Radio galaxies and the XRB are, indeed, correlated with each other (Boughn 1998).

An important source of noise in the cross-correlation of Figure 7 is instrument noise of the *COBE* DMR receivers. In addition, the relatively poor angular resolution of the *COBE* radiometers reduces, somewhat, the amplitude of the ISW signal. Therefore, some improvement can be expected by repeating the analysis on future CMB maps, such as that soon to be produced by NASA's *Microwave Anisotropy Probe* (MAP) satellite mission. If such an analysis still finds the absence of an ISW effect, then the current Λ CDM model would be in serious conflict with observational data if the X-ray bias can be similarly constrained. On the other hand, a positive detection would provide important evidence about the dynamics of the universe even if the X-ray bias remains uncertain.

8. CONCLUSIONS

By carefully reconstructing the *HEAO* beam and analyzing its autocorrelation function, we have been able to confirm the presence of intrinsic clustering in the XRB. This gives independent verification of the multipole analysis of Scharf et al. (2000), and the level of clustering we see is comparable. The clustering we see is in excess of that predicted by standard CDM models and indicates that some biasing is needed. The amount of biasing required depends on the

cosmological model and on how the bias evolves over time; if the bias is constant, typical models indicate that $b_X \simeq 2$. The biases of galaxies, clusters of galaxies, radio sources, and quasars have yet to be adequately characterized, so whether or not the above X-ray bias is excessive is a question that, for the present, remains unanswered.

We have also confirmed, at the 2–3 σ level, the detection of the Compton-Getting dipole in the XRB due to the Earth's motion with respect to the rest frame of the CMB. However, we have been unable to confirm the presence of an intrinsic dipole in the XRB and have actually been able to exclude a significant part of the range reported by Scharf et al. (2000). While our dipole limit is still too small to conflict with any of the favored CDM models, combining our dipole limit with observations of the local bulk flow enables us to constrain $\Omega_m^{0.6}/b_X(0) > 0.24$. For constant-bias models, this suggests a relatively large matter density, as is also seen in other velocity studies; however, the uncertainty in this limit is still considerable.

With the observed X-ray clustering, large Λ CDM models predict a detectable correlation with the CMB arising via the integrated Sachs-Wolfe effect. That we have not

observed this effect suggests $\Omega_\Lambda \lesssim 0.60$. This is beginning to conflict with models preferred by a combination of CMB, large-scale structure, and supernova Ia data (e.g., de Bernardis et al. 2000; Bahcall et al. 1999).

This work gives strong motivation for further observations of the large-scale structure of the hard X-ray background. Better measurements of the full-sky XRB anisotropy are needed, as is more information about the redshift distribution of the X-ray sources. This will be essential for cross-correlation with the new CMB data from the *MAP* satellite and to bridge the gap between the CMB scales and those probed by galaxy surveys such as Two Degree Field and Sloan Digital Sky Survey.

We would like to acknowledge Keith Jahoda, who is responsible for constructing the *HEAO 1 A-2* X-ray map and who provided us with several data-handling programs. We also thank Neil Turok for useful discussions, Ed Groth for a variety of analysis programs, and Steve Raible for his help with some of the analysis programs. R. C. acknowledges support from a PPARC Advanced Fellowship. This work was supported in part by NASA grant NAG5-9285.

REFERENCES

- Allen, J., Jahoda, K., & Whitlock, L. 1994, *Legacy*, 5, 27
 Bahcall, N. Ostriker, J. P., Perlmutter, S., & Steinhardt, P. 1999, *Science*, 284, 1481
 Barcons, X., Carrera, F. J., Ceballos, M. T., & Mateos, S. 2001, in AIP Conf. Proc. 599, X-Ray Astronomy: Stellar Endpoints, AGN, and the Diffuse X-Ray Background, ed. N. E. White, G. Malaguti, & G. G. C. Palumbo (Melville: AIP), 3
 Boldt, E. 1987, *Phys. Rep.*, 146, 215
 Bond, J. R., Jaffe, A., & Knox, L. 1998, *Phys. Rev. D*, 57, 2117
 Boughn, S. 1998, *ApJ*, 499, 533
 ———. 1999, *ApJ*, 526, 14
 Boughn, S., & Crittenden, R. 2002, *Phys. Rev. Lett.*, 88, 1302
 Boughn, S., Crittenden, R., & Turok, N. 1998, *NewA*, 3, 275 (BCT)
 Carrera, F., et al. 1993, *MNRAS*, 260, 376
 Comastri, A., Setti, G., Zamorani, G., & Hasinger, G. 1995, *A&A*, 296, 1
 Compton, A., & Getting, I. 1935, *Phys. Rev.*, 47, 817
 Cowie, L., et al. 2002, *ApJ*, 566, L5
 Cress, C. M., & Kamionkowski, M. 1998, *MNRAS*, 297, 486
 Crittenden, R., & Turok, N. 1996, *Phys. Rev. Lett.*, 76, 575
 Davis, M., Tonry, J., Huchra, J., & Latham, D. 1980, *ApJ*, 238, L113
 de Bernardis, P., et al. 2000, *Nature*, 404, 955
 Fry, J. N. 1996, *ApJ*, 461, L65
 Gendreau, K. C., et al. 1995, *PASJ*, 47, L5
 Giacconi, R., et al. 2001, *ApJ*, 551, 624
 Gilli, R., Salvati, M., & Hasinger, G. 2001, *A&A*, 366, 407
 Giommi, P., Perri, M., & Fiore, F. 2000, *A&A*, 362, 799
 Haslam, C. G. T., et al. 1982, *A&AS*, 47, 1
 Iwan, D., et al. 1982, *ApJ*, 260, 111
 Jahoda, K. 1993, *Adv. Space Res.*, 13 (12), 231
 Jahoda, K., & Mushotzky, R. 1989, *ApJ*, 346, 638
 Kneissl, R., & Smoot, G. 1993, *COBE Note* 5053
 Lahav, O., Piran, T., & Treyer, M. A. 1997, *MNRAS*, 284, 499
 Lahav, O., Santiago, B., Webster, A., Strauss, M., Davis, M., Dressler, A., & Huchra, J. 2000, *MNRAS*, 312, 166
 Lahav, O., et al. 2002, *MNRAS*, 333, 961
 Miyaji, T. 1994, Ph.D. thesis, Univ. Maryland
 Miyaji, T., Lahav, O., Jahoda, K., & Boldt, E. 1994, *ApJ*, 434, 424
 Mushotzky, R., & Jahoda, K. 1992, in *The X-Ray Background*, ed. X. Barcons & A. C. Fabian (Cambridge: Cambridge Univ. Press), 80
 Mushotzky, R. F., Cowie, L. L., Barger, A. J., & Arnaud, K. A. 2000, *Nature*, 404, 459
 Peebles, P. J. E. 1993, *Principles of Physical Cosmology* (Princeton: Princeton Univ. Press)
 Piccinotti, G., Mushotzky, R. F., Boldt, E. A., Holt, S. S., Marshall, F. E., Serlemitsos, P. J., & Shafer, R. A. 1982, *ApJ*, 253, 485
 Rosati, P., et al. 2002, *ApJ*, 566, 667
 Scharf, C. A., Jahoda, K., Treyer, M., Lahav, O., Boldt, E., & Piran, T. 2000, *ApJ*, 544, 49
 Shafer, R. A. 1983, Ph.D. thesis, Univ. Maryland (NASA TM 85029)
 Soltan, A. M., Hasinger, G., Egger, R., Snowden, S., & Trümper, J. 1996, *A&A*, 305, 17
 Tegmark, M., & Peebles, P. J. E. 1998, *ApJ*, 500, L79
 Treyer, M. A., Scharf, C. A., Lahav, O., Jahoda, K., Boldt, E., & Piran, T. 1998, *ApJ*, 509, 531
 Tully, R. B. 1988, *Nearby Galaxies Catalog* (Cambridge: Cambridge Univ. Press)
 Vikhlinin, A., & Forman, W. 1995, *ApJ*, 455, L109
 Voges, W., et al. 1996, *IAU Circ.*, 6420, 2
 White, R., & Stemwedel, S. 1992, in *ASP Conf. Ser. 25, Astronomical Data Analysis Software and Systems I*, ed. D. Worrall, C. Biemesderfer, & J. Barnes (San Francisco: ASP), 379
 White, M., & Bunn, E. F. 1995, *ApJ*, 450, 477